The Astrophysical Journal, 580:763–773, 2002 December 1

CHANDRA X-RAY SPECTROSCOPY AND IMAGING OF THE GALAXY CLUSTER PKS 0745−191

Amalia K. Hicks, Michael W. Wise, John C. Houck, and Claude R. Canizares
Massachusetts Institute of Technology, Center for Space Research, 1 Hampshire Street, Building NE80-6007, Cambridge, MA 02139-4307;
ahicks@alum.mit.edu, wise@space.mit.edu, houck@space.mit.edu, crc@space.mit.edu
Received 2002 March 21; accepted 2002 August 2

ABSTRACT

We present a detailed spectral and spatial analysis of the galaxy cluster PKS 0745−191, using recent observations from the *Chandra X-Ray Observatory*. The data provide information on the temperature and metallicity of the intracluster medium, the distribution of emission throughout the cluster, morphology of the cluster core, and an independent mass estimate that can be compared to that from gravitational lensing. X-ray spectra extracted from the central 300 kpc (∼2′) are well described by a two-temperature plasma, and the mean cluster temperature is consistent with previously determined values. The distribution of both temperature and metallicity within the inner 360 kpc (2.′3) of PKS 0745−191 is probed on scales of 8″ (∼20 kpc), yielding a relatively constant abundance throughout the region and a strong temperature gradient (down to ∼4–5 keV) within the central 215 kpc. β-model fits to the surface brightness profile of PKS 0745−191 indicate that a second β-model component is required to fit the inner ∼10 kpc. Imaging analysis of the cluster core reveals an irregular morphology within the inner 50 kpc and confirms that the X-ray emission peak lies within 0.″5 (the spatial resolution of *Chandra*) of both the optical and radio central cD positions. The cluster mass, based on both two-temperature and multiphase fits to the X-ray spectrum, is in close agreement with lensing mass estimates of PKS 0745−191.

Subject headings: cooling flows — galaxies: clusters: individual (PKS 0745−191) — gravitational lensing — X-rays: galaxies

1. INTRODUCTION

As the largest gravitationally bound objects in the universe, clusters of galaxies are important tracers of the large-scale distribution of matter. Because the distribution of clusters depends sensitively on the underlying cosmology (Evrard 1990; Frenk et al. 1990; Richstone, Loeb, & Turner 1992; Navarro, Frenk, & White 1995; Eke, Cole, & Frenk 1996), improved tests of cosmological models require accurate measurements of the properties of many individual clusters. The masses of galaxy clusters and their internal matter distribution are of particular interest. Three primary observational techniques have been widely used to derive the mass distribution in galaxy clusters: measurements of the galaxy velocity dispersion, modeling of gravitational lensing effects, and examination of X-ray emission from hot intracluster gas.

Most early measurements of cluster masses were based on optical observations of the motion of cluster galaxies. These measurements are complicated by the fact that cluster membership for individual galaxies is often uncertain. Furthermore, although determination of cluster masses from the galaxy velocity dispersion is founded on the assumption that the cluster is virialized, the virialization requirement is often unsatisfied. Many clusters are dynamically young and unrelaxed because the dynamical timescale for cluster formation is comparable to the Hubble time (Richstone et al. 1992).

Gravitational lensing studies infer the cluster mass from measurements of distortions produced in images of background galaxies. Lensing studies have the advantage that they directly measure the total projected mass in all forms along the line of sight. In particular, the lensing mass includes both luminous and dark matter, independent of assumptions about the dynamical state of the cluster (Tyson, Valdes, & Wenk 1990; Kaiser & Squires 1993). However, lensing measurements give no information on the dynamical state of the cluster or the relative amounts of luminous and dark matter or the segregation of baryonic matter between galaxies and intracluster hot gas.

X-ray observations of clusters provide complementary data, yielding a measure of the cluster mass that is independent of mass concentrations along the line of sight and also, through the plasma temperature map, yielding information on the dynamical state of the cluster (Mathiesen & Evrard 2001). The intracluster gas provides a useful probe of the cluster mass because the gas rapidly attains hydrostatic equilibrium in the cluster potential. In equilibrium, the gas temperature is typically in the range 10^7–10^8 keV, making the gaseous intracluster medium a prodigious source of thermal X-ray emission. Using X-ray observations to measure the gas density and temperature and assuming spherical symmetry, the radial mass distribution, $M(r)$, can be derived from the condition of hydrostatic equilibrium

$$M_{\rm tot}(< r) = -\frac{kTr}{\mu m_p G}\left(\frac{d\ln\rho_{\rm gas}}{d\ln r} + \frac{d\ln T}{d\ln r}\right), \qquad (1)$$

where $\rho_{\rm gas}$ is the gas density and T is the gas temperature. Detailed simulations indicate that the assumption of hydrostatic equilibrium can yield reasonably accurate cluster masses even in cases in which the cluster has not completely relaxed, although the exact range of validity of this approach remains uncertain (Schindler 1996; Evrard, Metzler, & Navarro 1996; Anninos & Norman 1996; Eke, Navarro, & Frenk 1998).

Along with their cosmological implications, X-ray observations of galaxy clusters are also motivated by interest in the origin and evolution of the gaseous intracluster medium itself. One question that has been the focus of intensive effort for a number of years concerns the fate of the X-ray–emitting gas. In a large fraction of dynamically relaxed clus-

ters, the radiative cooling time of gas in the cluster core is short compared to the Hubble time. In the absence of a heat source capable of balancing losses due to cooling, the intracluster gas is expected to settle inward in a "cooling flow" (see, e.g., Sarazin 1988; Fabian 1994). Previous X-ray estimates of the cooling rates ($\dot{M}$) revealed many clusters with $\dot{M} > 100\ M_\odot\ \mathrm{yr}^{-1}$ and, in some cases, as high as $\dot{M} \sim 1000\ M_\odot\ \mathrm{yr}^{-1}$. Once it cools below X-ray–emitting temperatures, the fate of the gas is unclear, but given the amount of material involved, some observable signature is expected. Sustained over a Hubble time, these cooling rates imply the accumulation of greater than $10^{12}\ M_\odot$ of material, but detailed examination of clusters at many wavelengths has so far failed to confirm the amount of cooling material inferred from X-ray observations or to reveal its final state.

Allen, Fabian, & Kneib (1996) and Allen (1998) have argued that the presence of a cooling flow can have an important effect on the cluster mass determination. Recent comparisons between cluster masses determined from X-ray observations and from gravitational lensing have revealed disagreements in the sense that the lensing value is sometimes larger than the X-ray–determined value. However, Allen et al. (1996) have argued that, at least for relaxed clusters, better agreement can be obtained if the presence of a cooling flow is taken into account.

The luminous cluster PKS 0745−191 is an excellent example. Using X-ray observations from *ASCA* and *ROSAT*, Allen et al. (1996) report that PKS 0745−191 contains one of the largest known cooling flows, with a mass deposition rate of $\sim$1000 $M_\odot\ \mathrm{yr}^{-1}$. From optical observations, they also report the discovery of a bright arc consistent with gravitational lensing of a galaxy at redshift $z = 0.433$. Using the lensing data, they derive the projected mass of the central part of the cluster, finding good agreement with the corresponding mass obtained from a multiphase analysis of the X-ray data. They emphasize, however, that a multiphase analysis is required; their single-phase analysis of the *ASCA* data clearly disagrees with their lensing result, yielding a mass that is smaller than the lensing value by a factor of $\sim$3.

In this paper we present our analysis of high angular resolution X-ray imaging observations of PKS 0745−191 using the *Chandra X-Ray Observatory*. From these data we derive mass estimates and cooling flow mass deposition rates. X-ray surface brightness and abundance profiles are also presented, along with a map of the projected plasma temperature distribution. In addition, we compare our high-resolution X-ray image of the cluster core with observations in the optical and radio.

Throughout this paper we used $H_0 = 50\ \mathrm{km\ s^{-1}\ Mpc^{-1}}$, $\Omega_M = 1.0$, $\Omega_\Lambda = 0.0$, and $q_0 = 0.5$. For PKS 0745−191 we take the redshift to be $z = 0.1028$, so that the luminosity distance $D = 631$ Mpc, and $1''$ corresponds to a linear distance of 2.57 kpc.

2. OBSERVATIONS

PKS 0745−191 was observed twice using *Chandra*/HETGS. The first of these observations, observation ID (ObsID) 510, occurred on 1999 October 14, when the temperature of the ACIS focal plane was −110°C. The second observation (ObsID 1509) was on 2000 March 4 at a focal plane temperature of −120°C. There was a 208° difference in roll angle between the two observations.

The ACIS gain was corrected using the most recent calibration files available, taking into account the focal plane temperature of the instrument during each observation. The aspect solutions were examined for irregularities, but none were found. Background contamination due to charged particle flares was reduced by removing time intervals during which the background rate exceeded the average background rate by more than 20%. The event files were filtered on standard grades, and bad pixels were removed using standard cleaning procedures. After filtering, the net remaining exposure times were 44,784 and 38,999 s, respectively.

We fitted a two-dimensional elliptical Lorentzian to the counts image of each data set to locate the center of the X-ray emission peak and measure its ellipticity. The center positions of the two observations differ in declination by $3''$, apparently as the result of an astrometry error in pipeline processing. For this reason, our imaging analysis used only the more recently reprocessed observation, ObsID 510. Our spectral analysis is unaffected by the offset.

Using ObsID 510, the centroid of the flux-corrected X-ray emission lies at $\alpha = 07^{\mathrm{h}}47^{\mathrm{m}}31\overset{\mathrm{s}}{.}3 \pm 0\overset{\mathrm{s}}{.}5$, $\delta = -19°17'40\overset{''}{.}0 \pm 0\overset{''}{.}5$ (J2000.0), the exact coordinates of the cD galaxy. The axis ratio is 0.65 ± 0.06, with the major axis at a position angle of $99° \pm 3°$, measured counterclockwise on the sky from north.

The zeroth-order image is sufficiently extended that it overlaps with events from the dispersed spectra. This overlap has no effect on the cluster core, becoming significant only at a radius of $75''$ from the center of the zeroth-order image. The cross-dispersion extent of the overlap region was measured by fitting Gaussians to the cross-dispersion profiles. To remove the overlap, we excised the region beginning $75''$ (193 kpc) along the dispersion direction from the cluster center and extending to approximately 2 σ in the cross-dispersion direction on either side of the axis of the dispersed spectrum. Within a radius of $2\overset{'}{.}3$ (360 kpc) any remaining contamination lies at a very low level and is restricted to energies $E > 4$ keV along the MEG dispersion direction and $E > 8$ keV along the HEG dispersion direction.

3. SPECTRAL ANALYSIS

Chandra's unparalleled spatial resolution makes it possible to examine spatial variations in the X-ray emission on much smaller scales than were previously accessible. In this section we present our analysis of the structure of the inner $2\overset{'}{.}3$ (360 kpc) of PKS 0745−191. We also discuss a similar analysis of the emission-weighted mean spectrum that may be directly compared with results from lower resolution observations.

3.1. *Integrated Spectrum Analysis*

Spectra were extracted from both data sets in an elliptical region with a $2'$ ($\sim$300 kpc) major axis and an ellipticity of 0.35, centered on the X-ray emission peak. These extractions yielded spectra with 56,863 counts and 47,288 counts for ObsIDs 510 and 1509, respectively. These spectra were then analyzed with XSPEC (Arnaud 1996) using response matrice files (RMFs) and effective area files (ARFs) generated from the latest version of the *Chandra* calibration data-

TABLE 1

COMPARISON OF INTEGRATED SPECTRAL FITS FOR $R < 300$ kpc

Model	kT (keV)	$N_{\rm H}$ ($\times 10^{21}$ cm^{-2})	Z ($Z_\odot$)	$\dot{M}$ ($M_\odot$ yr^{-1})	$kT_{\rm low}$ (keV)	χ^2/dof
Single T.....	$6.9^{+0.2}_{-0.2}$	4.24	$0.43^{+0.04}_{-0.04}$	...	...	1101/931
	$8.1^{+0.4}_{-0.4}$	$3.4^{+0.1}_{-0.1}$	$0.49^{+0.05}_{-0.05}$	...	...	988/930
Double T.....	$8.7^{+0.5}_{-0.5}$	4.24	$0.52^{+0.05}_{-0.05}$	...	$1.2^{+0.1}_{-0.1}$	946/929
	$8.8^{+0.5}_{-0.5}$	$4.1^{+0.3}_{-0.3}$	$0.52^{+0.05}_{-0.05}$	...	$1.3^{+0.1}_{-0.2}$	945/928
Single T plus cooling flow...	$12.1^{+3.00}_{-0.7}$	4.24	$0.55^{+0.06}_{-0.06}$	970^{+67}_{-59}	0.001	947/930
	$12.1^{+3.6}_{-0.9}$	$4.27^{+0.09}_{-0.09}$	$0.55^{+0.06}_{-0.06}$	985^{+72}_{-55}	0.001	947/929

base (CALDB 2.7); the RMF includes the improved calibration for the low-energy response of the aim point CCD on ACIS-S. For all analyses, a single RMF was generated at the position of the X-ray centroid and used for analysis of the entire region. Variations in the spectral resolution of the ACIS-S aim point CCD were found to be smaller than 10% within the extraction region; fits using RMFs taken from other points in the region gave equivalent results within the errors. Variations in the effective area were negligible within the extraction region. Backgrounds were extracted for these observations from the aim point chip (ACIS-S3). The background regions were chosen as far away from the aim point as possible and were sized to minimize contamination by diffracted photons. Each spectrum was grouped to contain at least 20 counts bin^{-1}, and data from the two observations were fitted simultaneously.

The spectra were fitted with three models, each including foreground absorption: a single-temperature model, a two-temperature model, and a single-temperature plus cooling flow model. Each of the spectral models was fitted twice, once with the absorbing column frozen at its measured value of 4.24×10^{21} cm^{-2} (Dickey & Lockman 1990), and once allowing the absorption to vary. The cluster redshift was fixed throughout the analysis. Data below 0.5 keV were excluded from the fits as a result of uncertainties in the ACIS calibration, while energies above 8.0 keV were neglected as a result of background contamination. The results of these spectral fits, along with 90% confidence ranges, are shown in Table 1.

Of the models considered, the best fits were obtained with two-temperature MEKAL and multiphase MKCFLOW plasma models. A plot of the fit to the two-temperature model is shown in Figure 1. For this model, we find an

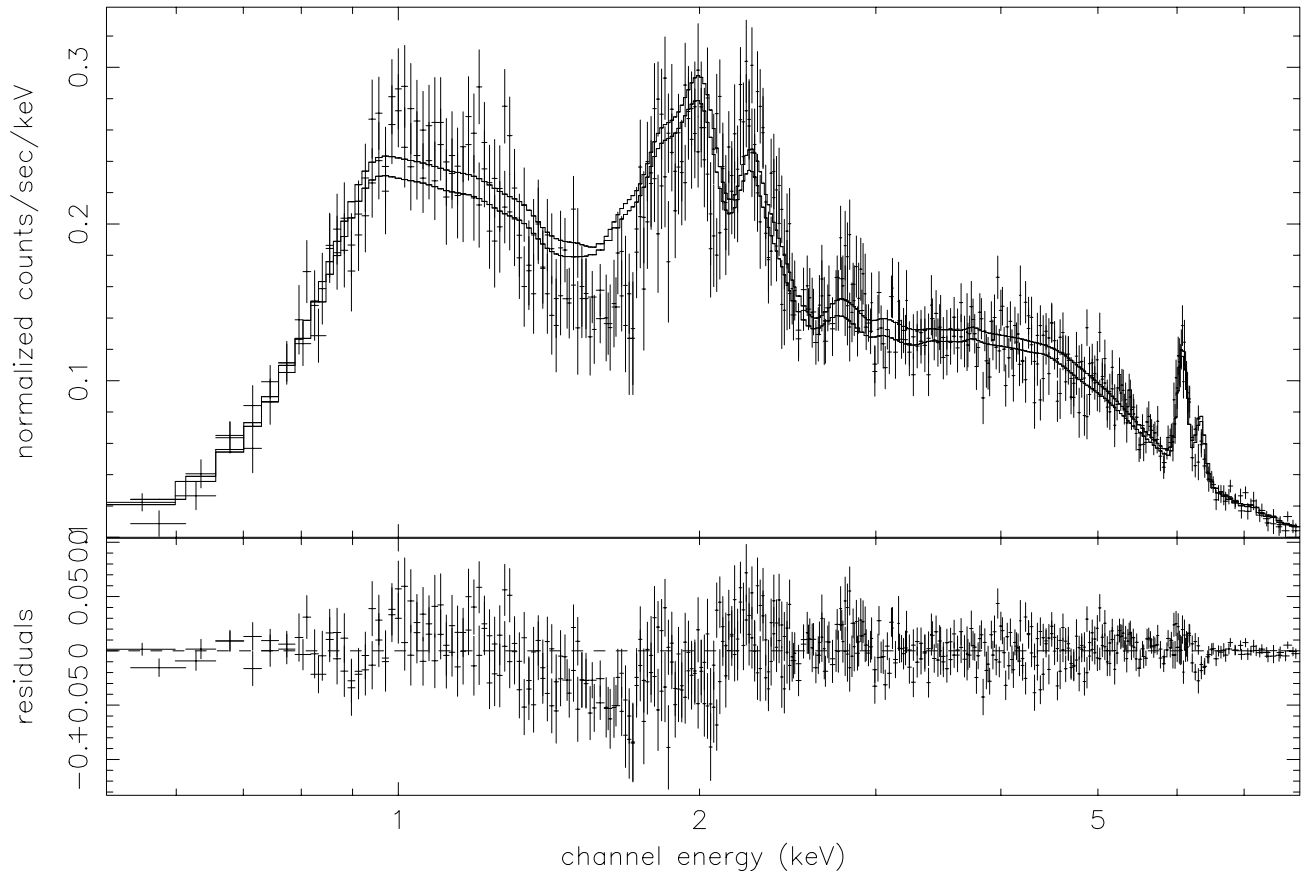

FIG. 1.—XSPEC plots showing a spectrum fit with a two-temperature model. This fit resulted in an ambient cluster temperature of $8.7^{+0.5}_{-0.5}$ keV, a low-temperature component of $1.2^{+0.1}_{-0.1}$ keV, an abundance of $0.52^{+0.05}_{-0.05}$ $Z_\odot$, and a reduced χ^2 of 1.02 for 929 dof. The spectrum was extracted from a circle centered on the emission peak with a radius of 2′ (∼300 kpc) and was grouped to include 100 counts bin^{-1} for clarity.

ambient cluster temperature of $8.7^{+0.5}_{-0.5}$ keV, a low-temperature component of $1.2^{+0.1}_{-0.1}$ keV, and an abundance of $0.52^{+0.05}_{-0.05}$ $Z_{\odot}$. The reduced χ^2 for this fit was 1.02 for 929 degrees of freedom (dof). These results are consistent with both the 0′–2′ *ASCA* cooling flow analysis of Allen et al. (1996) and the 0′–2′ *BeppoSAX* multiphase analysis of PKS 0745−191 (De Grandi & Molendi 1999).

The larger residuals between 1.3 and 2 keV (Fig. 1) appear to be the result of a calibration problem, most likely associated with spatial variations in the RMF combined with interpolation errors on the rather coarse energy grid used in the RMF calibration. Similar residuals are seen in observations of other clusters, generally appearing in cases in which spectra have been extracted from a source that spans several of the detector regions where calibration data are specified. These residuals do not significantly affect our fit results.

3.2. *Spatially Resolved Spectra*

To investigate the radial dependence of temperature and abundance in PKS 0745−191, spectra were extracted from 12 elliptical annuli spanning the central 2.′3 (360 kpc) of the cluster. Figure 2 shows the spectral extraction regions overlaid on an adaptively smoothed counts image of the cluster. The extraction regions were sized to ensure at least 3000 counts per spectrum in the 0.29–7.0 keV band for each data set. The extracted spectra were grouped to contain 20 counts bin^{-1} and analyzed using XSPEC. Models were fitted to data over the energy range 0.6–7.0 keV. ARFs, RMFs, and backgrounds used were the same as described in § 3.1, and data from the two observations were again fitted simultaneously at each radius.

The same plasma models described in § 3.1 were again used to fit the data. While single-temperature spectral models generally fitted the data well (reduced χ^2 of 0.98–1.55), adding a cooler component in fits to the nine innermost spectra (the central 215 kpc of the cluster) improved the fits somewhat. Outside of that region, the normalization of the low-temperature component of the two-temperature model was consistent with zero, and single-temperature models provided equally good fits to the data. The cooling flow model did not constrain the temperature outside of the innermost region.

Because of large discrepancies in spatial resolution, it is difficult to compare prior work on the spatial structure of PKS 0745−191 to the results reported in this section. However, it is worth noting that our results differ in some respects.

In their *BeppoSAX* analysis, De Grandi & Molendi (1999) ruled out a large temperature gradient in PKS 0745−191, but our investigation shows that there is indeed a noticeable gradient present in the central region (Figs. 3 and 4). Their work also supports a strong abundance gradient, but we see no indication of such a gradient in the inner 360 kpc (2.′3) of the cluster. Instead, we find that the abundance remains relatively constant throughout the core (Fig. 5), with an average value of ∼0.5 $Z_{\odot}$, consistent with their result for the inner 2′. The results of Allen et al. (1996) are also consistent with a constant metal abundance although they favor a somewhat lower value of ∼0.3.

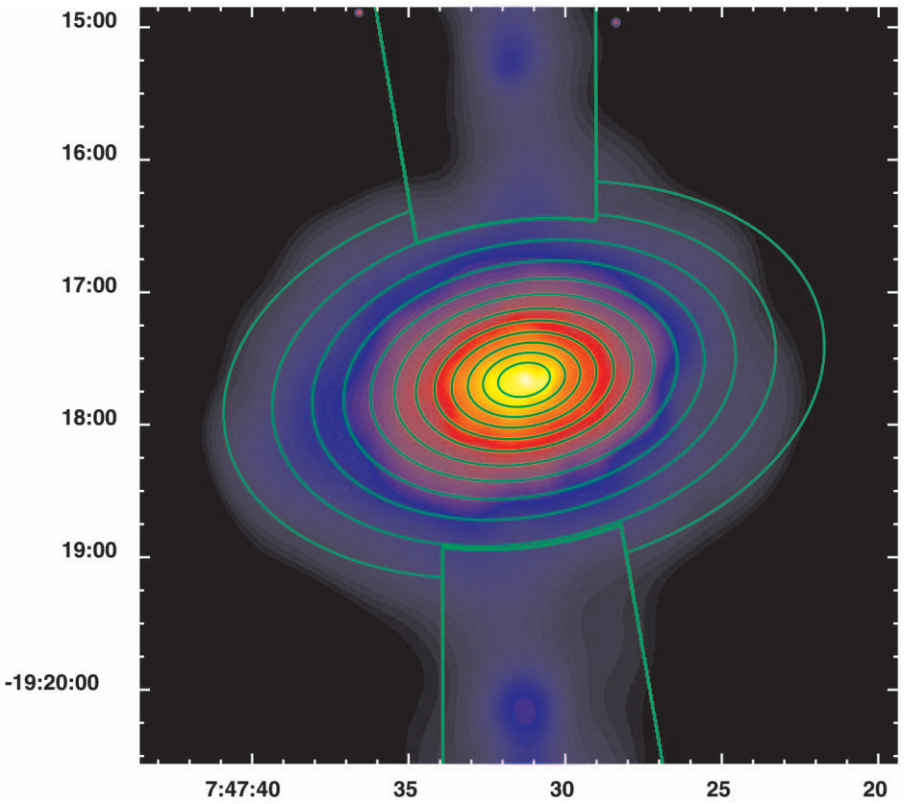

FIG. 2.—Adaptively smoothed image of the core of PKS 0745−191, made from the longer of the two observations. Contours highlight elliptical regions from which spectra were extracted to produce temperature and abundance profiles, along with regions excluded from our spectral analysis as a result of possible diffracted photon contamination. The peak of emission lies within 0.″5 (the spatial resolution of *Chandra*) of the cD galaxy.

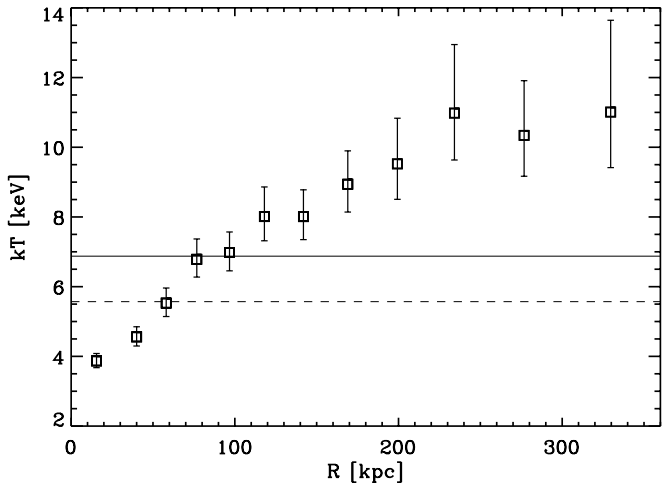

FIG. 3.—Radial temperature profile determined by fitting, in XSPEC, single-temperature spectral models to spectra extracted from elliptical annuli selected to include a minimum of 3000 counts in the 0.29–7.0 keV band (see Fig. 1). Error bars represent 90% confidence limits. The solid line represents the temperature obtained by fitting 0′–2′ *Chandra* data with a single-temperature model. The dotted line indicates the temperature reported by Allen et al. (1996) as a result of their 0′–2′ (∼310 kpc) single-temperature *ASCA* analysis of PKS 0745−191.

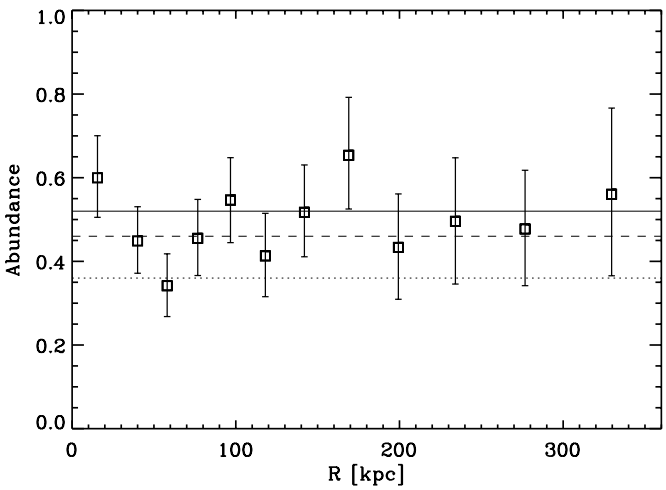

FIG. 5.—Abundance profile determined with a single-phase spectral model. The abundances that we present here are consistent (within their errors) with the corresponding abundances resulting from our two-temperature analysis. Although not as well constrained as the temperature profile, our analysis is consistent with a constant abundance of roughly 0.5 $Z_{\odot}$ throughout the inner region of PKS 0745−191. The solid line is the abundance value resulting from a 0′–2′ two-temperature analysis, the dashed line is the *BeppoSAX* 0′–2′ cooling flow model result, and the dotted line represents the outcome of the *ASCA* multiphase analysis of that same region.

3.3. *Temperature Maps*

Extending the radial analysis discussed above, we have generated maps of the plasma temperature in the central regions of the cluster. These maps were computed for both data sets independently using a custom module within the ISIS (Houck & Denicola 2000) spectral analysis package that automates the process of extracting many pulse invariant spectra, generating appropriate ARFs and RMFs for each spectrum, and then fitting a given spectral model (for a detailed description see J. C. Houck, D. S. Davis, & M. W. Wise 2002, in preparation).

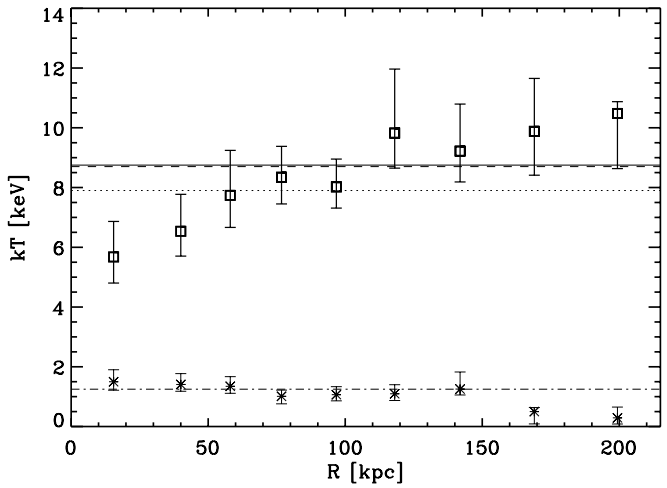

FIG. 4.—Radial temperature profile determined by fitting a two-temperature spectral model to spectra extracted from the elliptical annuli discussed in Fig. 3. Error bars represent 90% confidence limits. The solid line indicates the best-fitting (high) temperature from a 0′–2′ *Chandra* two-temperature analysis of this cluster, and the dot-dashed line illustrates the best-fitting low-temperature component of the same analysis. The dashed line represents the value quoted from the *BeppoSAX* cooling flow analysis of the inner 2′ of PKS 0745−191, and the dotted line indicates the *ASCA* SIS-0 cooling flow model result for the same region. The low-temperature component of the two-temperature models could not be constrained at radii larger than 215 kpc (1.′4).

In generating the temperature maps, a grid of adaptively sized extraction regions was selected to contain a minimum of 2000 counts in the 0.3–7.0 keV band. The grid was selected to span a 200″ × 200″ region centered on the cluster peak, consistent with the integrated spectrum analysis described above. We avoid problems associated with chip edge effects by choosing spectral extraction regions that lie entirely within the edges of the ACIS-S3 chip. The extracted spectra were fitted with a MEKAL plasma model including foreground Galactic absorption fixed at the nominal value of 4.24×10^{21} cm^{-2}. The abundance was fixed at a value of 0.5 as determined by the integrated spectral fits. Single-parameter 90% confidence limits were computed for each fit to estimate the level of statistical uncertainty in each pixel of the temperature map. Although the temperature map shown in Figure 6 was computed holding the absorbing column and metal abundance fixed, similar results were obtained when the absorbing column and metal abundance were allowed to vary.

The temperature map for the central 100″ × 100″ region of PKS 0745−191 (ObsID 510) is shown in Figure 6. In general, the resulting temperature structure is consistent with the radial temperature profile presented in Figure 3. The overall temperature morphology traces the X-ray surface brightness. The region of coolest emission, with temperatures ∼3–4 keV, appears to be centered at a slight offset from the position of the central cD. However, this scale is comparable to the map resolution in the core and so may be consistent with a zero offset. Finally, we find no evidence for gas cooler than ∼3 keV, consistent with results from other cooling flows observed with *Chandra* and *XMM* (Peterson et al. 2001; M. W. Wise et al. 2002, in preparation).

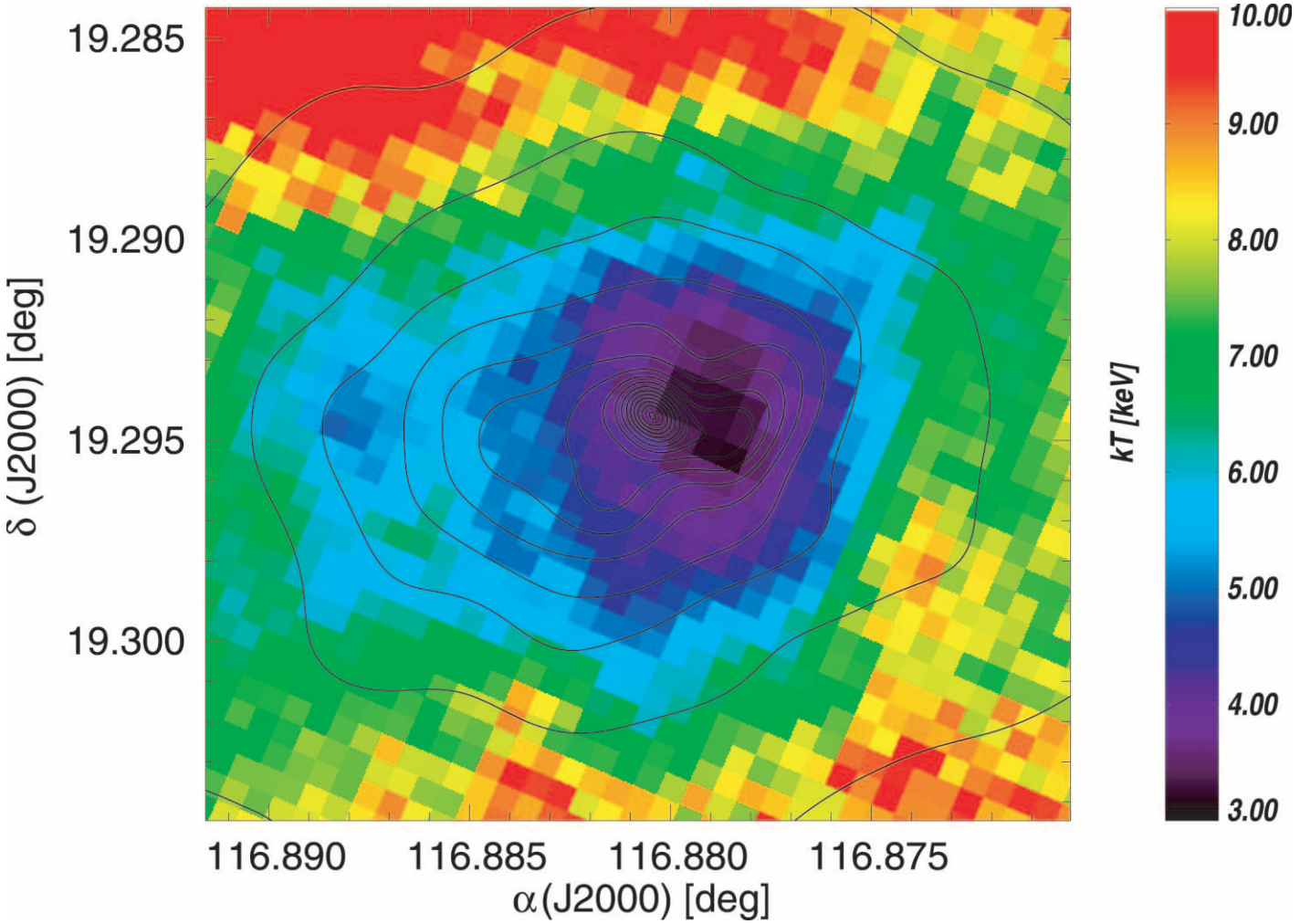

FIG. 6.—Temperature map for the central 100″ × 100″ region of PKS 0745−191 (ObsID 510) centered on the peak of cluster emission. The contours show the adaptively smoothed X-ray surface brightness. The color bar indicates the temperature scale in keV. The statistical error in the map is ~0.8 keV at the 90% confidence level.

4. SURFACE BRIGHTNESS

Radial surface brightness profiles were computed for each observation. To minimize errors due to the energy dependence of the effective area, we divided the 0.29–7.0 keV bandpass into 12 bands in which the effective area is roughly constant. In each energy band, we extracted a 2048 × 2048 image of the undispersed zero-order counts. We also computed a zero-order exposure map for each energy band. After excising regions affected by contamination from dispersed counts, the surface brightness was computed in elliptical annuli with centroid, position angle, and axis ratio given in § 2. All quoted radii are measured along the semimajor axis.

The surface brightness profiles from each data set were mutually consistent within their errors. In each energy band, the surface brightness profiles from each data set were fitted simultaneously, once with a single β-model and once with a double β-model. The single β-model has the form

$$I(r) = I_B + I_0\left(1 + \frac{r^2}{r_0^2}\right)^{-3\beta+1/2}, \qquad (2)$$

where I_B is a constant representing the intensity contribution of the background, I_0 is the normalization, and r_0 is the core radius. The double β-model has the form

$$I(r) = I_B + I_1\left(1 + \frac{r^2}{r_1^2}\right)^{-3\beta_1+1/2} + I_2\left(1 + \frac{r^2}{r_2^2}\right)^{-3\beta_2+1/2}, \qquad (3)$$

where each component has fit parameters (I_k, r_k, β_k).

Table 2 shows the results of fitting a single β-model to those energy bands that have sufficient signal-to-noise ratio

TABLE 2
β-MODEL FITS

E (keV)	$R_{\rm core}$ (arcsec)	β	I_0[a]	I_B[a]	χ^2/dof
0.29–7.00...	$18.0^{+0.4}_{-0.6}$	$0.47^{+0.01}_{-0.01}$	3919^{+104}_{-88}	11^{+2}_{-2}	616.3/476
0.29–2.00...	$15.2^{+0.9}_{-0.9}$	$0.48^{+0.01}_{-0.01}$	2677^{+126}_{-120}	8^{+1}_{-1}	557.8/476
2.00–7.00...	$19.6^{+0.9}_{-0.9}$	$0.47^{+0.01}_{-0.01}$	1761^{+57}_{-54}	$5.6^{+1.3}_{-0.9}$	567.3/476
0.54–1.00...	13^{+1}_{-1}	$0.48^{+0.01}_{-0.02}$	828^{+77}_{-80}	$3.6^{+1.5}_{-0.6}$	427.5/476
1.00–1.57...	16^{+1}_{-1}	$0.49^{+0.01}_{-0.01}$	1054^{+71}_{-68}	$1.3^{+0.9}_{-0.2}$	532.4/476
1.57–2.00...	17^{+2}_{-1}	$0.48^{+0.02}_{-0.01}$	553^{+41}_{-38}	$1.5^{+0.6}_{-0.2}$	504.2/476
2.00–3.50...	19^{+1}_{-1}	$0.48^{+0.01}_{-0.01}$	1009^{+47}_{-44}	$2.7^{+0.9}_{-0.4}$	574.6/476
3.50–5.00...	23^{+2}_{-1}	$0.48^{+0.01}_{-0.01}$	353^{+18}_{-18}	$1.3^{+0.6}_{-0.2}$	439.8/476
5.00–7.00...	22^{+2}_{-2}	$0.47^{+0.02}_{-0.02}$	298^{+20}_{-19}	$1.3^{+0.7}_{-0.2}$	513.6/476

[a] Surface brightness I in units of 10^{-9} photons s^{-1} cm^{-2} arcsec^{-2}.

TABLE 3
DOUBLE β-MODEL FITS

E (keV)	R_{c1} (arcsec)	β_1	I_{01}[a]	R_{c2} (arcsec)	β_2	I_{02}[a]	I_B[a]	χ^2/dof
0.29–7.00...	$1.5^{+0.7}_{-0.2}$	$0.41^{+0.13}_{-0.05}$	3819^{+603}_{-637}	20^{+1}_{-1}	$0.49^{+0.02}_{-0.01}$	3367^{+258}_{-225}	14^{+2}_{-2}	553.7/473
0.29–2.00...	$2.3^{+1.3}_{-0.4}$	$0.45^{+0.09}_{-0.07}$	2227^{+217}_{-304}	17^{+2}_{-1}	$0.49^{+0.02}_{-0.01}$	1907^{+864}_{-318}	10^{+2}_{-2}	536.1/473
2.00–7.00...	$1.1^{+0.2}_{-0.2}$	$0.41^{+0.15}_{-0.05}$	1583^{+91}_{-158}	21^{+2}_{-1}	$0.49^{+0.02}_{-0.01}$	1959^{+933}_{-326}	7^{+1}_{-1}	535.3/473

[a] Surface brightness I in units of 10^{-9} photons s^{-1} cm^{-2} arcsec^{-2}.

to constrain the parameters. Although a single β-model yields a reasonably good fit to the surface brightness profile, it fails to account for a significant excess of emission in the cluster core. Adding a second β-component (Table 3) yields a better fit to the surface brightness profile (Fig. 7), consistent with the findings of Ikebe et al. (1999) and Xue & Wu (2000).

The double β-model yields the best fit to the 0.29–7.0 keV data giving $\beta = 0.49^{+0.02}_{-0.01}$ (at large radius), a core radius of $51.42^{+2.57}_{-2.57}$ kpc, and a background value of 1.4×10^{-8} photons s^{-1} cm^{-2} arcsec^{-2}, with a reduced χ^2 of 1.15 for 473 dof. Although the core radius of our best-fitting single β-model is comparable to the 37.5 ± 5 kpc core radius reported by Allen (1998), the outer core radius of the double β-model is significantly larger.

5. IMAGING ANALYSIS

5.1. *Substructure*

We used an unsharp masking technique to examine the substructure in the cluster core. By subtracting a heavily smoothed, flux-corrected image (I_S) from an adaptively smoothed, full-resolution image (I_F), we effectively subtract out the smooth, large-scale structure leaving residuals associated with smaller scale inhomogeneities.

A full-resolution 400×400 pixel image centered on the X-ray emission peak was extracted from ObsID 510 in the 0.29–7.0 keV band. A matching zero-order exposure map was constructed for the same region. Regions contaminated by dispersed photons were removed from both the image and exposure map, and the resulting image was adaptively smoothed using the CIAO tool CSMOOTH. A similar image was smoothed with a Gaussian kernel of 20 pixel (10″) FWHM. Each of the two resulting images was divided by the exposure map and exposure time, to produce flux-corrected images. The residual image, ($I_F - I_S$), with hardness contour overlays is shown in Figure 8.

Substructure is clearly present in the core of PKS 0745, with excess emission covering an elongated area of about 100 kpc × 50 kpc. The brightest point in this image lies directly on the cD galaxy at the center of the cluster and has a surface brightness that is 68% of the adaptively smoothed surface brightness at that point.

Similar images were made in a hard band (H: 2.0–7.0 keV) and a soft band (S: 0.29–2.0 keV). These images showed no appreciable difference in the morphology of the core substructure, although the relatively low signal-to-noise ratio is not sensitive to weak temperature variations.

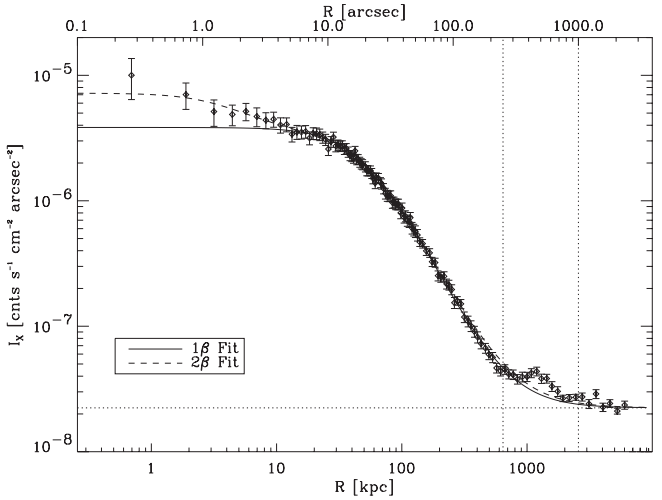

FIG. 7.—Radial surface brightness for the 0.29–7.0 keV band accumulated in 1″ annular bins. A solid line traces the best single β-model fit, and the dashed line illustrates the improved fit obtained by fitting these data with a double β-model. The horizontal dotted line represents the best-fitting background value. Two vertical dotted lines indicate a region of data that was not included in the fit, as a result of residual contamination from first-order grating photons. The remaining data were well fitted by a double β-model with an inner core radius of 1″.5 (3.86 kpc) and β-value of 0.41 and an outer core radius of 20″ (51.42 kpc) and β-value of 0.49.

5.2. *Hardness Map*

Images with the same specifications as those mentioned in § 5.1 were made of both the hard band (H) and the soft band (S). These images were smoothed using the smoothing scale produced in the analysis of the full energy band (0.29–7.0 keV). Using exposure maps calculated for the individual bands, and following the procedure detailed in § 5.1, smoothed, flux-corrected images were constructed. Using these flux-corrected images I_H and I_S, we constructed a hardness map ($\mathscr{H}$), defined as

$$\mathscr{H} \equiv \frac{I_S - I_H}{I_S + I_H}. \quad (4)$$

Contours of the resulting hardness ratio image ($\mathscr{H}$) are overlayed on the core residuals map of Figure 8.

Although the hardness contours are less elongated than the residuals image, ellipticity is clearly present. Soft emission is peaked in two places, neither of which corresponds exactly to the position of the cD, although the more central of the soft emission peaks lies within 3″ of it.

5.3. *Optical and Radio Comparisons*

The adaptively smoothed core image (I_F) from § 5.1 was used to construct a set of 10 X-ray isophotes, spaced logarithmically over a range in surface brightness from

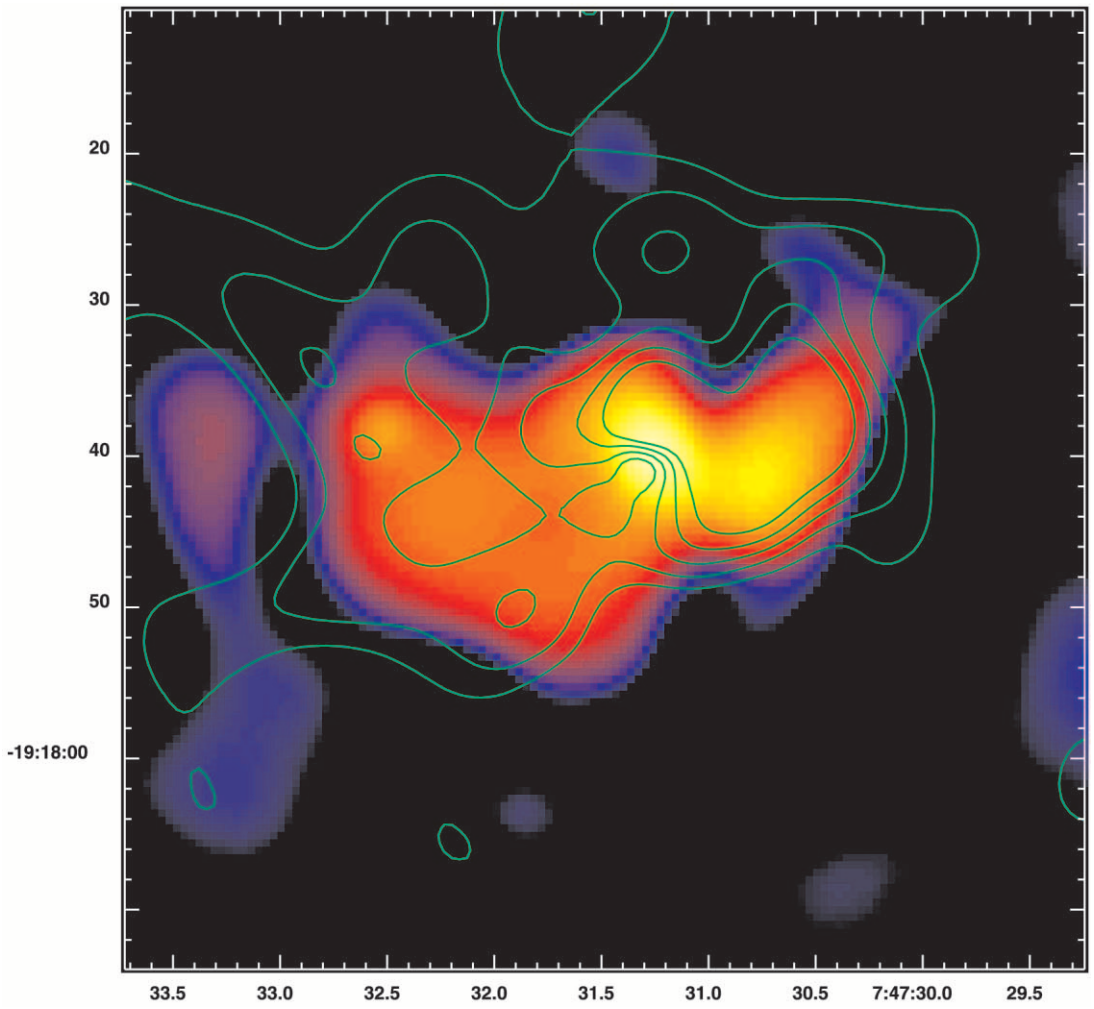

FIG. 8.—Image of PKS 0745−191 indicating core substructure. A highly smoothed image of this region was subtracted from an adaptively smoothed image of PKS 0745−191 to enhance X-ray substructure in the core. The peak of emission lies at the location of the cD galaxy and has a surface brightness that is 65% of the adaptively smoothed surface brightness at that point. Five contours of constant hardness ratio (§ 5.2) are spaced linearly over the range 0.06–0.18 and illustrate variations in the value $(I_S - I_H)/I_{\rm tot}$.

2.2×10^{-8} to 1.8×10^{-6} photons s^{-1} cm^{-2} pixel^{-2}. Figure 9 shows these contours overlaid on a *Hubble Space Telescope* (*HST*) optical image of PKS 0745−191 obtained from the *HST* archive.

Ten isophotes were also constructed with the 8350 MHz VLA radio image of PKS 0745−191 (Taylor, Barton, & Ge 1994), logarithmically spaced over the range 1×10^{-4} to 1×10^{-2} Jy beam^{-1}. Figure 10 shows these radio contours overlaid on the adaptively smoothed core image (I_F) from § 5.1.

Figures 9 and 10 show that the X-ray emission peak of PKS 0745−191 lies within 0.″5 (the spatial resolution of *Chandra*) of both the optical and radio centers of the cD galaxy. This is consistent with the *ROSAT* result of Allen et al. (1996), who found that their X-ray emission peak corresponded to the optical position of the cD within the point-spread function of *ROSAT* (∼5″).

Examination of the center of the optical image reveals that the major axis of the cD is misaligned with the X-ray isophotes, although the optical and X-ray contours are well correlated on larger scales. In contrast, the radio morphology does not appear correlated with the X-ray emission. An anticorrelation between X-ray and radio morphology has been seen in some nearby clusters of galaxies (McNamara et al. 2000), but these data do not clearly show this effect.

The brightest of the gravitational arcs of PKS 0745−191 can be seen in the optical image as a faint streak directly to the right of the cluster. There seems to be no apparent connection between the X-ray emission and the arcs.

6. MASS DETERMINATION

6.1. *Density and Cooling Time*

A cluster of galaxies whose X-ray surface brightness profile follows a β-model is consistent with a gas density distribution of the form

$$n_{\rm gas}(r) = n_0 \left(1 + \frac{r^2}{r_c^2}\right)^{-3\beta/2}, \qquad (5)$$

where n_0 is the cluster central density. This relation assumes isothermal, hydrostatic equilibrium in spherical symmetry. X-ray spectral fits determine both plasma temperature and, via the emission measure, the central density.

Spectra were extracted from an elliptical aperture with a 0.5 Mpc major axis, which was centered on the X-ray

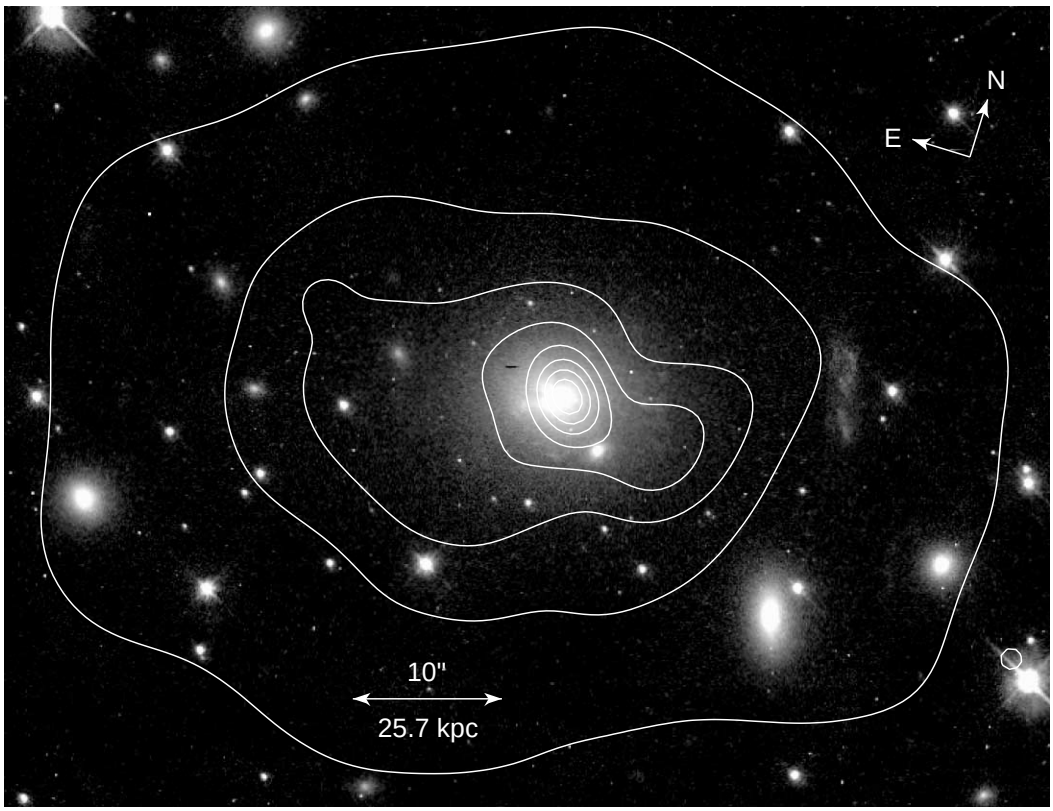

FIG. 9.—*HST* image of PKS 0745−191, spanning the wavelength range 4789.0–6025.0 Å. *Chandra* X-ray isophotes (see § 5.1 for details) from an adaptively smoothed core image, composed of data from ObsID 510 in the 0.29–7.0 keV range, are overlaid in white. The X-ray peak is within 0″.5 of the optical center of the cD galaxy. Note the presence of the gravitational arc directly to the right of the cD.

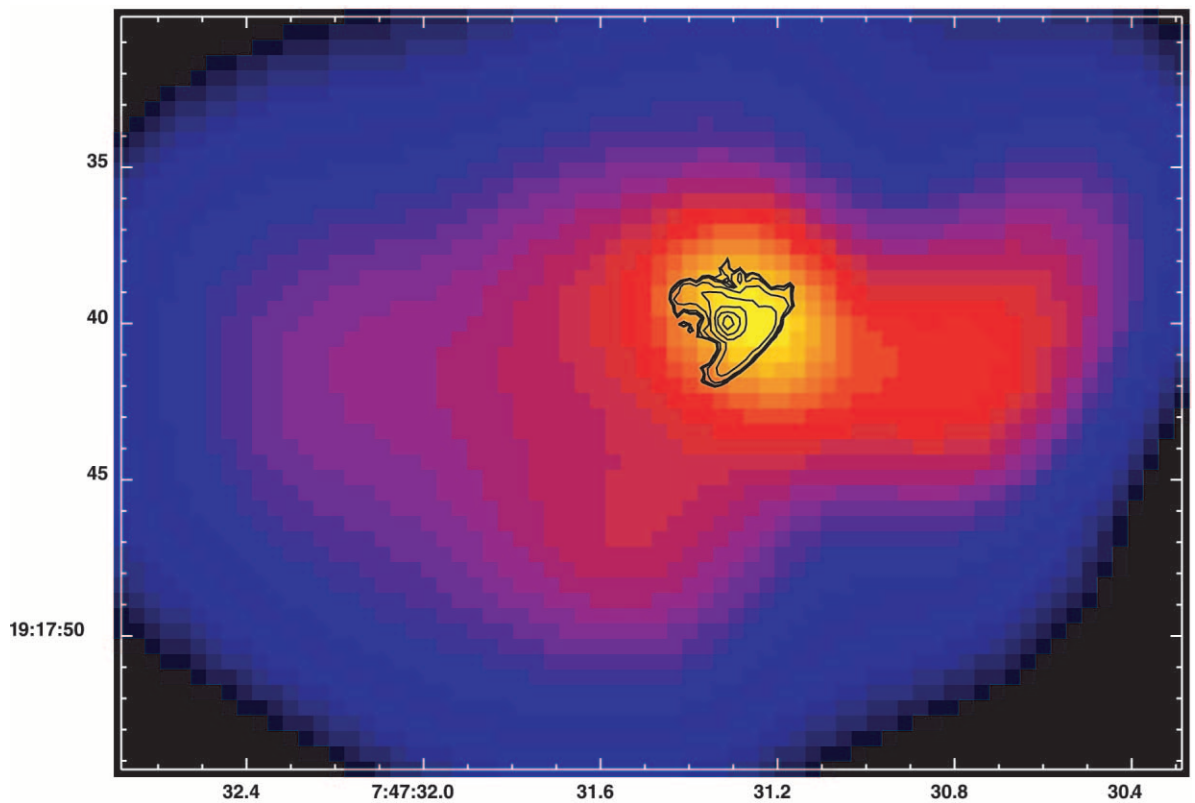

FIG. 10.—Adaptively smoothed X-ray image, composed of data from ObsID 510 in the 0.29–7.0 keV range. VLA radio contours (Taylor et al. 1994; see § 5.1 for details) of PKS 0745−191 are overlaid in black. The peak of X-ray emission lies within 0″.5 of the central radio source.

TABLE 4
MASS ESTIMATES FOR $R < 0.5$ Mpc

Model	kT (keV)	n_0 (cm^{-3})	$M_{\rm gas}$ ($\times 10^{13}\,M_\odot$)	$M_{\rm tot}$ ($\times 10^{13}\,M_\odot$)	$M_{\rm arc}$ ($\times 10^{13}\,M_\odot$)
Single T.....	$7.6^{+0.3}_{-0.3}$	$0.070^{+0.001}_{-0.001}$	$5.6^{+0.5}_{-0.4}$	$18.9^{+1.0}_{-0.9}$	$1.9^{+0.1}_{-0.1}$
Double T.....	$10.0^{+0.8}_{-0.9}$	$0.069^{+0.001}_{-0.001}$	$5.5^{+0.4}_{-0.4}$	$24.8^{+2.1}_{-2.1}$	$2.5^{+0.2}_{-0.2}$
Single T plus cooling flow...	$12.08^{+0.01}_{-0.78}$	$0.069^{+0.001}_{-0.001}$	$5.5^{+0.4}_{-0.4}$	$29.1^{+1.4}_{-1.3}$	$2.9^{+0.1}_{-0.1}$

emission peak. The spectra were grouped into 20 count bins, and the 0.5–8.0 keV data were fitted in XSPEC with the same calibration files, backgrounds, and models employed in § 3.1. The resulting best-fit temperatures (using the higher temperature from the two-temperature model) and computed central densities are given in Table 4.

The characteristic time that it takes a plasma to cool isobarically through an increment of temperature δT can be written as

$$\delta t_{\rm cool} = \frac{5}{2}\frac{k}{n\Lambda(T)}\delta T, \tag{6}$$

where n is the electron density, $\Lambda(T)$ is the total emissivity of the plasma (the cooling function), and k is Boltzmann's constant. For isochoric cooling, $5/2$ is replaced by $3/2$.

Using this expression, the distribution of cooling times can be derived from the cluster density profile. The radius at which the cluster cooling time is equal to the cluster age (generally assumed to be a large fraction of the Hubble time) is defined as the cooling radius. Using $H_0 = 50$, $q_0 = 0.5$, the assumption of isobaric cooling, our β-model fit parameters, and the fit results of the cooling flow model, we determined the cooling radius and central cooling time of PKS 0745−191. For a cluster age of 1×10^{10} yr, and using the cooling function appropriate to a $0.5\,Z_\odot$ abundance plasma, we get a cooling radius of 104 kpc and a central cooling time of 8.67×10^8 yr in the cluster core.

Allen et al. (1996) calculate a cooling radius of 180^{+11}_{-9} kpc from a *ROSAT* HRI observation and 212^{+52}_{-23} kpc from *ROSAT* PSPC data. Using a deprojection analysis, they derive somewhat longer cooling times of 1.95×10^9 and 1.11×10^9 yr, respectively. However, their analysis assumed an ambient cluster temperature of 10 keV, and the sizes of the central bins from which they extract cooling times are relatively large: 15″ for the PSPC and 8″ for the HRI. Given that our results are roughly consistent at a radius of 200 kpc, the detailed differences probably arise from a combination of the ∼2 keV temperature difference and the difference in the bin size.

6.2. *Mass Comparisons*

Optical *HST* images indicate the presence of a gravitational lensing arc at a radius of 45.9 kpc from the center of PKS 0745−191. This arc, likely due to lensing of an early-type spiral galaxy at a redshift of 0.433, has a length of ∼15.″5 and width of ∼3.″5. From a detailed lensing analysis Allen et al. (1996) derived a spherically projected mass of 3.0×10^{13} $M_\odot$ and an elliptical mass estimate of $(2.1\text{–}2.5) \times 10^{13}\,M_\odot$ within the tangential critical radius.

Using our β-model fit parameters, the spectral fitting results of Table 4, equation (2), and the equation of hydrostatic equilibrium (eq. [1]), we have computed various mass estimates for PKS 0745−191. Table 4 gives the gas mass within 0.5 Mpc of the core, the total mass within 0.5 Mpc, and the lensing mass. Lensing mass estimates were calculated for a cylindrical region with radius 45.9 kpc and an assumed cluster extent of 1 Mpc. Extending the cluster further does not significantly affect the results.

The X-ray mass estimate based on a multiphase analysis is consistent with spherical optical mass estimates, while the two-temperature model provides a mass comparable to elliptical lensing estimates. In contrast, the single-temperature model clearly underestimates the mass. Our cooling flow–derived lensing mass estimate is consistent with that reported by Allen (1998).

6.3. *Mass Estimates*

Although it provides an excellent description of the X-ray surface brightness profile (see Fig. 6), the hydrostatic, isothermal, spherically symmetric β-model is an obvious oversimplification, given the observed temperature gradient and elliptical morphology. Nevertheless, the mass estimates are relatively insensitive to these details.

Evrard (1990) investigated the accuracy of mass estimates based on the β-model using a large number of cosmological gasdynamic simulations of cluster formation and evolution. He concluded that β-model mass estimates are reasonably accurate when computed for regions with mean density ($\bar{\rho}$) between 500 and 2500 times the critical density ($\rho_c = 3H_0^2/8\pi G$). Using our mass estimates (see Table 4), the region inside a 0.5 Mpc radius has a mean density of $\bar{\rho} \gtrsim 1300 h^{-2}\rho_c$, placing it within the hydrostatic region commonly seen in cluster evolution simulations.

Using his simulations, Evrard (1990) also found that the presence of a temperature gradient has a relatively small effect on the mass determination. After including the known three-dimensional temperature gradient from the simulated clusters, the corresponding mass estimates for regions with $\bar{\rho} \gtrsim 500$ changed by less than 1 σ. This is consistent with the conclusion obtained by comparing the sizes of the temperature and density gradients in equation (1). Both the single-temperature fits and the hotter component of the two-temperature fits give a temperature gradient of about $d \ln T / d \ln r \approx 0.3$ at a radius of 200 kpc. For comparison, the β-model indicates a gas density gradient of $d \ln \rho_g / d \ln r \approx 1.3$ at the same radius. Therefore, in estimating the total mass within this radius, the temperature gradient is at most a 25% effect.

A somewhat larger source of uncertainty arises from the cluster's elliptical shape. Although the morphology may be more complex, we can estimate the uncertainty due to projection effects by computing the gas mass for oblate and prolate mass distributions suitably oriented and normalized so that the surface brightness and axis ratio match the observations. For an axis ratio of 0.6, the estimated gas mass could vary by as much as ∼50% depending on the geometry,

although the extremes of this range require coincidental alignment, making them less likely.

7. SUMMARY AND DISCUSSION

We have presented our analysis of *Chandra* observations of the galaxy cluster PKS 0745−191. These data provide a much clearer picture of the X-ray structure of the central 300 kpc. The spectra are not well fitted by a single-temperature model because of excess soft emission from the core. The cluster-integrated spectrum is best fitted by a two-temperature model with temperatures of $8.7^{+0.5}_{-0.5}$ and $1.2^{+0.1}_{-0.1}$ keV, with an abundance of $0.52^{+0.05}_{-0.05}$ $Z_{\odot}$. Consistent with results from other *Chandra* observations of cooling flows, we see no evidence for X-ray emission from cooling gas with temperatures below ~2–3 keV (Peterson et al. 2001; M. W. Wise et al. 2002, in preparation).

Chandra's excellent angular resolution has allowed us to study the distribution of both metallicity and temperature on very small scales (~20 kpc) in the inner 360 kpc of PKS 0745−191. Using single-temperature spectral models, we find an ostensibly constant abundance with a value of ~0.5 $Z_{\odot}$ and a steep temperature gradient within the innermost 215 kpc.

Imaging analysis of the cluster core reveals enhanced X-ray emission from an elongated region in the core of about 100 kpc × 50 kpc. The hardness ratio map shows a somewhat larger region ($R > 50$ kpc) of excess soft emission (0.29–2.0 keV) in the core. Comparison of the X-ray data to optical (*HST*) and radio (VLA) observations of PKS 0745−191 places the X-ray emission peak within 0.″5 of both the optical and radio central cD positions.

The surface brightness profile is best fitted by a double β-model with an outer core radius of 51.42 kpc and β-value of 0.49. The central density is $n_0 = 0.069^{+0.001}_{-0.001}$. The central cooling time based on a multiphase cooling flow model is 8.67×10^8 yr, with a corresponding cooling radius of 104 kpc.

We found best agreement between the X-ray and spherical gravitational lensing masses using a multiphase spectral model for which we obtained a mass of 2.9×10^{13} $M_{\odot}$. Single-temperature models imply masses consistently smaller than lensing mass estimates. Mass results stemming from two-temperature models, although smaller than spherical lensing estimates, are consistent with elliptically derived values. In any case, our X-ray spectra require no more than two temperature components and, in particular, do not require a multiphase treatment of the sort emphasized by Allen et al. (1996). Although the physics of cooling gas strongly suggests that a multiphase medium should be present, our data do not require it.

We thank Greg Taylor for providing access to his radio observations of PKS 0745−191.

REFERENCES

Allen, S. W. 1998, MNRAS, 296, 392
Allen, S. W., Fabian, A. C., & Kneib, J. P. 1996, MNRAS, 279, 615
Anninos, P., & Norman, M. L. 1996, ApJ, 459, 12
Arnaud, K. A. 1996, in ASP Conf. Ser. 101, Astronomical Data Analysis Software and Systems V, ed. G. H. Jacoby & J. Barnes (San Francisco: ASP), 17
De Grandi, S., & Molendi, S. 1999, A&A, 351, L45
Dickey, J. M., & Lockman F. J. 1990, ARA&A, 28, 215
Eke, V. R., Cole, S., & Frenk, C. S. 1996, MNRAS, 282, 263
Eke, V. R., Navarro, J., & Frenk, C. S. 1998, ApJ, 503, 569
Evrard, A. 1990, ApJ, 363, 349
Evrard, A. E., Metzler, C. A., & Navarro, J. F. 1996, ApJ, 469, 494
Fabian, A. C. 1994, ARA&A, 32, 277
Frenk, C. S., White, S. D. M., Efstathiou, G., & Davis, M. 1990, ApJ, 351, 10
Houck, J. C., & Denicola, L. A. 2000, ASP Conf. Ser. 216, Astronomical Data Analysis Software and Systems IX, ed. N. Manset, C. Veillet, & D. Crabtree (San Francisco: ASP), 591
Ikebe, Y., Makishima, K., Fukazawa, Y., Tamura, T., Xu, H., Ohashi, T., & Matsushita, K. 1999, ApJ, 525, 58
Kaiser, N., & Squires, G. 1993, ApJ, 404, 441
Mathiesen, B. F., & Evrard, A. E. 2001, ApJ, 546, 100
McNamara, B. R., et al. 2000, ApJ, 534, L135
Navarro, J., Frenk, C. S., & White, S. D. M. 1995, MNRAS, 275, 720
———. 2001, A&A, 365, L104
Richstone, D., Loeb, A., & Turner, E. L. 1992, ApJ, 393, 477
Sarazin, C. L. 1988, X-Ray Emission from Clusters of Galaxies (Cambridge: Cambridge Univ. Press)
Schindler, S. 1996, A&A, 305, 756
Taylor, G. B., Barton, E. J., & Ge, J. 1994, AJ, 107, 1942
Tyson, J., Valdes, F., & Wenk, R. 1990, ApJ, 349, L1
Xue, Y.-J., & Wu, X.-P. 2000, MNRAS, 318, 715